Manipulation of spatiotemporal photon distribution via chromatic aberration

Yuelin Li[1,*] and Sergey Chemerisov[2]

[1]*Accelerator Systems Division and Argonne Accelerator Institute, Argonne National Laboratory, Argonne, Illinois 60439, USA*

[2]*Chemical Science and Engineering Division, Argonne National Laboratory, Argonne, Illinois 60439, USA*

**Corresponding author: ylli@aps.anl.gov*

Received April 8, 2008; revised June 30, 2008; accepted July 2, 2008; posted July 30, 2008 (Doc. ID 94838); published August 28, 2008

We demonstrate a spatiotemporal laser-pulse-shaping scheme that exploits the chromatic aberration in a dispersive lens. This normally harmful effect transforms the phase modulation into a beam-size modulation at the focal plane. In combination with the intricate diffraction effect via beam apodization, this method provides a spatiotemporal control of photon distribution with an accuracy of diffraction limit on a time scale of femtoseconds. © 2008 Optical Society of America

OCIS codes: 320.5540, 140.3300.

Spatiotemporal control of ultrafast laser pulses is anticipated to have wide applications in coherence control of quantum systems, optical signal processing, laser-matter interaction, and generating electron beams for x-ray free-electron lasers [1,2] and ultrafast electron diffraction experiments [3]. However, spatiotemporal control is intrinsically complex owing to the difficulty in simultaneously controlling the spatial and time distribution and the fact that mature techniques normally work only in one domain [4–6]. Examples of high-fidelity shaping are sparse and achieved only in 2D shaping [7,8]. 3D control thus far has been achieved only via structured optics [9], temporal multiplexing via volume holography [10], or pulse stacking using multiple delay optics [11].

In this Letter, we demonstrate a spatiotemporal shaping technique based on the exploitation of the chromatic aberration, which normally destroys the focusing and imaging fidelity of an optical system and has to be carefully mitigated. In our scheme, however, it serves to couple the phase modulation in the time domain into the spatial domain, thus enabling simultaneous spatial and temporal manipulation.

The dependence of the refractive index upon the optical frequency gives rise to the chromatic aberration in a lens [12], where the change of the focal length due to a shift in frequency $\delta\omega$ is

$$\delta f = -\frac{f_0}{n_0-1}\chi\delta\omega, \tag{1}$$

where f_0 and n_0 are the nominal focal length and refractive index of the lens at ω_0. We assume a constant $\chi = \mathrm{d}n/\mathrm{d}\omega$. For a Gaussian beam, the beam size at the nominal focal plane is $w \approx w_0[1+(\delta f/z_R)^2]^{1/2}$. Here $w_0 = N\lambda_0/\pi$ is the beam waist at the nominal wavelength λ_0, with N being the NA, and $z_R = \pi w_0^2/\lambda_0$ is the Rayleigh range. It is obvious, therefore, if one can program $\delta\omega$ in time, one can also control the beam size in time. At $\delta f \gg z_R$, one has $w(t) \cong |\delta f(t)|/N$; thus the phase of the laser pulse is

$$\phi(t) = \pm\int \delta\omega(t)\mathrm{d}t = \pm\frac{n_0-1}{\chi}\frac{N}{f_0}\int w(t)\mathrm{d}t. \tag{2}$$

For a desired time-dependent intensity $I(t)$, the amplitude of the laser should be

$$A(t) \propto I(t)^{1/2}w(t). \tag{3}$$

One example of the spatiotemporal shape is the uniform ellipsoidal (UE) pulse desired for modern photoinjectors [13,14]. Such a laser pulse is expected to produce electron bunches with high charge and the lowest possible emittance [1,2], suitable for x-ray free-electron lasers and other electron-beam-based light sources.

To generate an ellipsoidal envelope with maximum radius of R and full length of $2T$, the transverse beam size as a function of time is $w(t) = R[1-(t/T)^2]^{1/2}$, which in turn gives the phase of the pulse using Eq. (2) [2]:

$$\phi(t) = -\omega_0 t \pm \frac{\Delta\omega}{2}\left[t\left(1-\left(\frac{t}{T}\right)^2\right)^{1/2} + T\sin^{-1}\frac{t}{T}\right], \tag{4}$$

where $\Delta\omega = (n_0-1)NR/\chi f_0$ is the maximum frequency shift. To keep the laser flux $|A(t)|^2/w(t)^2$ constant, we have [2]

$$A(t) = A_0\left[1-\left(\frac{t}{T}\right)^2\right]^{1/2}, \tag{5}$$

Equations (4) and (5) describe a pulse that can form a spatiotemporal ellipsoid at the focus of the lens [2]. The spatial temporal distribution can in general be image-relayed using achromatic optics to maintain the temporal-spatial fidelity, and the associated dispersion can be precompensated.

The above analysis is based on Gaussian optics and cannot treat the diffraction due to beam apodization, which is numerically evaluated using a Fourier optics model, such as the one elaborated in [15] and used in [2,16].

A proof-of-principle experiment is performed. The schematic of the experiment is shown in Fig. 1. A pair of Pockel cells is used to reduce the repetition rate of a Ti:sapphire oscillator from 90 MHz to 1 kHz. The 135 fs pulses after the Pockel cells are then split into two arms. One of them traverses a delay line to serve as a probe. The other, denoted as the main beam, is sent through an acousto-optic programmable dispersive filter (AOPDF) [5] and modulated in phase and amplitude. It is then spatially filtered to generate a Gausssian beam using a pair of achromatic lenses and a pinhole. A plano-spherical ZnSe lens (Janos Technology, A1204-105) is used for its high dispersion ($250\ \mathrm{fs}^2/\mathrm{mm}$ at 800 nm [17]) to form the desired spatiotemporal distribution at its focal plane, which is image relayed by an achromatic lens onto a 12-bit CCD camera to interfere with the probe beam. The interference fringes, as a function of delay between the two beams, are used to extract the spatiotemporal intensity distribution of the main beam. The imaging system is aligned to focus at 845 nm, accomplished by generating a narrowband beam of 2 nm at 845 nm via the AOPDF.

In the experiment, the AOPDF is set up according to Eqs. (4) and (5), with $T=1$ ps. In this setup, the wavelength of the pulse starts and ends at 845 nm, focused, but swings down to 790 nm, defocused, during the pulse. The second-order dispersion in all the optics and the third- and fourth-order dispersion in the AOPDF crystal are canceled by properly setting the AOPDF. The calculated (target) amplitude and phase in the time and frequency domain are given in Figs. 2(a) and 2(b) together with a spectrum measured in the experiment. The observed deviation between the measured and target spectra is attributed to the limited crystal length and slightly nonlinear response of the AOPDF across the spectrum. The transverse beam profile is given in Fig. 2(c), with a $1/e^2$ radius of 6 mm.

To extract the intensity of the main beam, we start with the signal recorded on the camera,

$$I(\mathbf{r}) = I_m(\mathbf{r}) + I_p(\mathbf{r}) + 2\cos(\omega[\tau + \delta(\mathbf{r})]) \int A_m(t,\mathbf{r}) A_p \times (t - \delta(\mathbf{r}) - \tau, \mathbf{r}) \cos[\phi_m(t) - \phi_p(t - \delta(\mathbf{r}) - \tau)] \mathrm{d}t, \tag{6}$$

where $A(\mathbf{r})$, $\phi(t)$, and $I(\mathbf{r}) = \int |A(t,\mathbf{r})|^2 \mathrm{d}t$ are the amplitude, phase, and integrated intensity of the laser beams, respectively; the subscripts m and p denote the main and probe beam, respectively; τ is the timing delay; and $\delta(\mathbf{r})$ is the additional location-dependent delay due to the angle between the two beams, respectively. The phase term in the integral, though impossible to evaluate for each location, only causes the interference fringes at the detector to shift. Therefore, if the probe pulse is much shorter than the main pulse, Eq. (6) can be reduced to

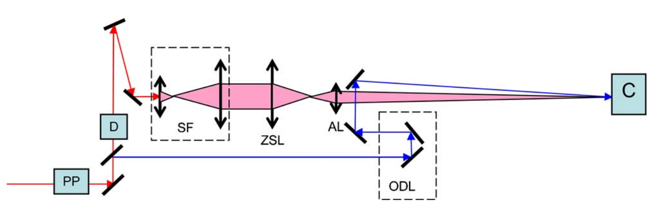

Fig. 1. (Color online) Schematic of the experiment. PP, pulse picker (a pair of Pockel cells); D, AOPDF; SF, achromatic spatial filter; ZSL, ZnSe lens; AL, achromatic image relay lens; ODL, optical delay line; C, camera.

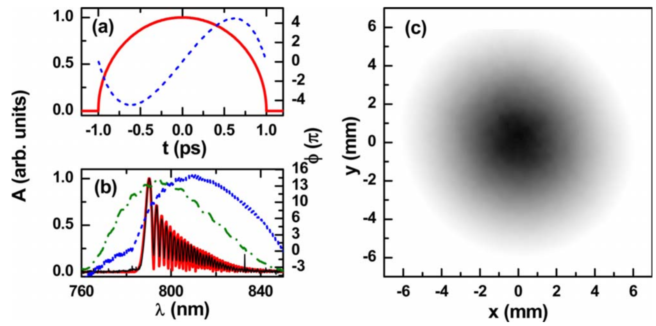

Fig. 2. (Color online) Laser pulse amplitude A (bold solid curves) and phase ϕ (dashed curves) calculated from Eqs. (5) and (6) in the (a) time and (b) frequency domain, and the measured spectrum amplitude [curve in (b)]. The thin solid transverse profile of the laser pulse after the spatial filter, in front of the ZnSe lens, is shown in (c) with a slightly diagonal elongation. The input laser spectrum is given in (b) as a dashed–dotted curve. The efficiency of the AOPDF is 5%. The linear phase has been subtracted to show the nonlinear nature.

$$I(\mathbf{r}) \approx I_m(\mathbf{r}) + I_p(\mathbf{r}) + 2\cos(\omega[\tau + \delta(\mathbf{r})]) \times \sqrt{\Delta t_p i_m(\tau,\mathbf{r})} \sqrt{I_p(\mathbf{r})}. \tag{7}$$

Here, Δt_p is the duration of the probe pulse, and $i(\tau,\mathbf{r}) = |A(\tau,\mathbf{r})|^2$ is the time-dependent intensity distribution. The second term describes the fringes as functions of delay and location, from which one can extract the contrast ratio $R(\tau,\mathbf{r})$, which in turn gives

$$i_m(\tau,\mathbf{r}) \propto R^2(\tau,\mathbf{r}) / I_p(\mathbf{r}). \tag{8}$$

Examples of the measured spatiotemporal intensity distributions are given in the left column of Fig. 3. The corresponding distributions from the Fourier model are given in the middle column, and an intensity lineout from both the experiment and simulation are shown in the right column. In the measurement an iris located directly in front of the ZnSe lens is adjusted to different sizes. A 3D isointensity surface plot comparison is given in Fig. 4 for the $a_0=3$ mm case.

As predicted by the Gaussian beam optics, the pulse shows generally an ellipsoidal envelope but with dramatic structure due to diffraction at the iris. With larger aperture size, the diffraction acquires higher and higher spatial frequency as can be seen from Figs. 3(a) and 3(b) and virtually becomes homogeneous at large aperture in simulations in [2]. We note that diffraction of ulrafast laser pulse remains an interesting research topic [18].

Though the agreement between the simulation and experiment is in general good, several discrepancies are noticed. The first is the better agreement at small aperture sizes. This is attributed to the limited dy-

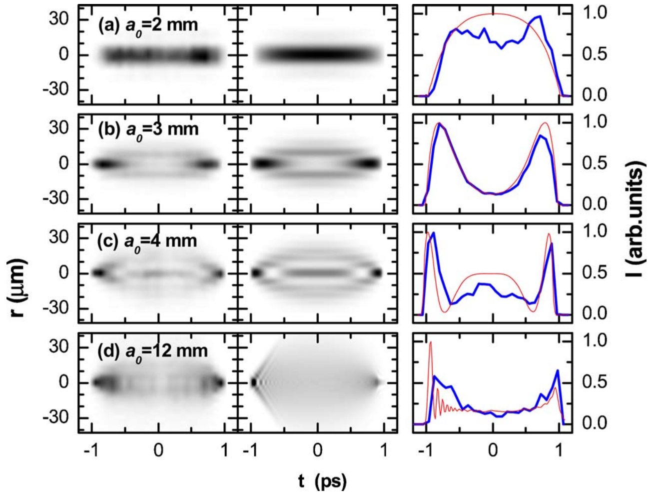

Fig. 3. (Color online) Measured (left column) and simulated (middle column) spatiotemporal intensity distribution with different iris radius a_0. The right column shows the corresponding measured (thick curves) and simulated (thin curves) intensity as function of time at $r=0$.

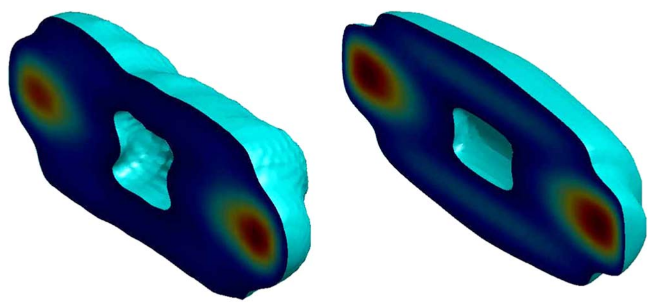

Fig. 4. (Color online) Cutaway view along the $t-r$ plane of the measured (left) and calculated (right) spatiotemporal isointensity surface plot of the pulse in Fig. 3(b).

namic range of the camera, which makes extraction of the signal difficult at low-intensity wings. In addition, the measurement suffers from pointing stability of the laser, which causes shot-to-shot fluctuation.

The temporal resolution of the measurement is limited by the probe-pulse duration at about 130 fs, and a shorter probe pulse would demand a higher dynamic range for data recording. Owing to the limited laser energy, we did not generate the larger (25 mm radius), top-hat transverse input profile needed for the ellipsoidal beam [2].

In summary, we demonstrated a scheme based on chromatic aberration for manipulating spatiotemporal photon distribution. Good agreement between measurement and simulation is achieved in a proof-of-principle experiment. The scheme is anticipated to be capable of adaptively generating high fidelity, femtosecond spatiotemporal, and submicrometer spatial control of a laser pulse. It is also expected to be able to generate 3D distributions with asymmetric apodization.

We thank D. Kaplan of Fastlite for fruitful discussions. The author also thanks K.-J. Kim and K. Harkay for support. This work is supported by the U.S. Department of Energy, Office of Science, Office of Basic Energy Sciences, under contract DE-AC02-06CH11357.

References

1. C. Limborg-Deprey and P. Bolton, Nucl. Instrum. Methods A **557**, 106 (2006).
2. Y. Li and J. W. Lewellen, Phys. Rev. Lett. **100**, 074801 (2008), and references therein.
3. P. Baum and A. H. Zewail, Proc. Natl. Acad. Sci. USA **103**, 16105 (2006), and references therein.
4. A. M. Weiner, Rev. Sci. Instrum. **71**, 1929 (2000).
5. F. Verluise, V. Laude, Z. Cheng, Ch. Spielmann, and P. Tournois, Opt. Lett. **25**, 575 (2000); product at http://www.fastlite.com.
6. See, e.g., *Laser Beam Shaping*, F. M. Dickey and S. C. Holswade eds. (Marcel Dekker, 2000).
7. J. C. Vaughan, T. Feurer, and K. A. Nelson, J. Opt. Soc. Am. B **19**, 2489 (2002).
8. M. C. Nuss and R. L. Morrison, Opt. Lett. **20**, 740 (1995).
9. R. Piestun and D. A. B. Miller, Opt. Lett. **26**, 1373 (2001).
10. K. B. Hill, K. G. Purchase, and D. J. Brady, Opt. Lett. **20**, 1201 (1995).
11. S. Zhou, D. Ouzounov, H. Li, I. Bazarov, B. Dunham, C. Sinclair, and F. W. Wise, Appl. Opt. **46**, 8488 (2007), and references therein.
12. M. Born and E. Wolf, *Principles of Optics* (Cambridge U. Press, 2003).
13. I. M. Kapchinskij and V. V. Vladimirskij, Conference on High Energy Accelerators and Instrumentation (CERN, Geneva, 1959), p. 274.
14. M. Reiser, *Theory and Design of Charged Particle Beams* (Wiley, 2005).
15. M. Kempe, U. Stamm, B. Wilhelmi, and W. Rudolph, J. Opt. Soc. Am. B **9**, 1158 (1992).
16. Y. Li and R. Crowell, Opt. Lett. **32**, 93 (2007).
17. Calculated from data in H. H. Li, J. Phys. Chem. Ref. Data **13**, 103 (1984).
18. S. P. Veetil, C. Vijayan, D. K. Sharma, H. Schimmel, and F. Wyrowski, J. Mod. Opt. **53**, 1819 (2006), and references therein.